PHOTONICS Research

Indefinite metacavities coupled to a mirror: bound states in the continuum with anomalous resonance scaling

Qiang Zhang,[1,2,*] Peixiang Li,[1] Zhiyuan Gu,[1] Shaoding Liu,[1,2] and Zejun Duan[1]

[1]College of Electronic Information and Optical Engineering, Taiyuan University of Technology, Taiyuan 030024, China
[2]Key Laboratory of Advanced Transducers and Intelligent Control System, Ministry of Education, Taiyuan University of Technology, Taiyuan 030024, China
*Corresponding author: zhangqiang02@tyut.edu.cn

Received 18 October 2023; revised 27 December 2023; accepted 15 January 2024; posted 17 January 2024 (Doc. ID 508159); published 1 March 2024

Indefinite metacavities (IMCs) made of hyperbolic metamaterials show great advantages in terms of extremely small mode volume due to large wave vectors endowed by the unique hyperbolic dispersion. However, quality (Q) factors of IMCs are limited by Ohmic loss of metals and radiative loss of leaked waves. Despite the fact that Ohmic loss of metals is inevitable in IMCs, the radiative loss can be further suppressed by leakage engineering. Here we propose a mirror coupled IMC structure which is able to operate at Fabry–Pérot bound states in the continuum (BICs) while the hyperbolic nature of IMCs is retained. At the BIC point, the radiative loss of magnetic dipolar cavity modes in IMCs is completely absent, resulting in a considerably increased Q factor (>90). Deviating from the BIC point, perfect absorption bands (>0.99) along with a strong near-field intensity enhancement ($>1.8 \times 10^4$) appear when the condition of critical coupling is almost fulfilled. The proposed BICs are robust to the geometry and material composition of IMCs and anomalous scaling law of resonance is verified during the tuning of optical responses. We also demonstrate that the Purcell effect of the structure can be significantly improved under BIC and quasi-BIC regimes due to the further enhanced Q factor to mode volume ratio. Our results provide a new train of thought to design ultra-small optical nanocavities that may find many applications benefitting from strong light–matter interactions.

https://doi.org/10.1364/PRJ.508159

1. INTRODUCTION

Optical metamaterials are man-made microstructures or nanostructures that can be designed to acquire optical properties out of the scope of natural materials [1–3]. The past few decades have witnessed the rapid development of optical metamaterials ranging from left-handed materials [4–6], zero-index materials [7,8], and ultra-high-index materials [9,10] to various functional metasurfaces [11,12]. Among them, hyperbolic metamaterials (HMMs) also known as indefinite metamaterials have attracted particular interest in recent years because of their promising applications in areas such as subwavelength far-field imaging [13], spontaneous emission engineering [14–16], and active devices [17]. The principal elements of the permittivity tensor of HMMs do not have the same sign, leading to a hyperboloidal iso-frequency surface (IFS) [18–20]. In principle, wave vectors in ideal HMMs can be infinitely large. Such a unique and intriguing property makes HMMs an excellent candidate for realizing ultra-small optical cavities of which the size can be shrunk to deep-subwavelength scale. Yao *et al.* theoretically studied the nanometer-scale optical cavities made of HMMs, namely indefinite metacavities (IMCs), and demonstrated that the size of IMCs can be as small as $(\lambda/20)^3$ (λ is the wavelength in vacuum) [21]. They further found that both resonance frequencies and quality (Q) factors of IMCs show anomalous scaling law with respect to cavity sizes. About one year after this work, three-dimensional IMCs configured as stacked metal–dielectric layers were theoretically and experimentally demonstrated by Yang *et al.* [22]. Inspired by these two pioneer works, much research focusing on applications of IMCs has been reported, such as surface-enhanced Raman spectroscopy [23], nonlinear optics [24,25], wave absorbers [26,27], microlasers and nanolasers [28,29], and optical and thermal radiation engineering [30–32].

Generally, many applications demonstrated in optical microcavities or nanocavities rely on the strength of light–matter interaction, which is basically determined by the ratio of Q factor to mode volume V_m, i.e., Q/V_m [33,34]. For IMCs, V_m can be extremely small due to the large wave vectors supported by HMMs [21,22]. However, nonradiative quality factor (Q_{nr})

of IMCs is inevitably limited by the Ohmic loss of metals, leading to total Q factor of reported IMCs smaller than 50 [21–23]. Notwithstanding, it is still possible to further reduce the radiative loss, in other words, improve the radiative quality factor Q_r of IMCs by structure design. Recently, optical bound states in the continuum (BICs) have gained much attention as they provide an appealing approach to obtain narrow optical resonances [35–37]. Theoretically speaking, an ideal BIC in a lossless system has an infinitely large Q factor and is completely decoupled to far fields [38–40]. When the BIC condition is slightly broken, BICs turn into quasi-BICs with finite but still high Q factors. For a system with dissipating materials, for example metals, upper limits of Q factors of BICs or quasi-BICs are restricted by Ohmic loss but the radiative loss can still be suppressed. Therefore, it is expected that IMCs working with BICs or quasi-BICs may show optical resonances that are not only endowed with boosted Q factors, but also bear the hyperbolic nature such as anomalous resonance scaling law and ultrasmall mode volume.

In this work, we present such attempts by placing arrays of IMCs made of stacked metal–dielectric layers on top of a reflecting mirror to realize Fabry–Pérot BICs. Similar to high-index nanoparticles or metal–insulator–metal resonators, IMCs also support in-plane magnetic modes that can couple to their images in the mirror [41–45]. We show that Fabry–Pérot BICs and quasi-BICs are obtained when the separation between IMCs and the reflecting mirror is appropriately tuned. As expected, the radiative damping rate (γ_r) of the mirror coupled IMC arrays depends on the separation and can be totally suppressed at the point of BIC. More importantly, mirror coupled IMCs can still be regarded as a cavity made of effective hyperbolic material and exhibit anomalous scaling law of the resonance wavelength with respect to their sizes. Meanwhile, the principle demonstrated here opens up the possibility of obtaining near-perfect absorption (PA) with IMCs where the critical coupling condition can be fulfilled via tuning γ_r to match it with the nonradiative damping rate (γ_{nr}). As a demonstration of strong light–matter interaction, we verify that the Purcell effect of IMCs can be enhanced by BICs and quasi-BICs. Our results provide a feasible scheme that combing IMCs and BICs to design ultra-small optical nanocavities with further enhanced Q/V_m for widespread applications.

2. RESULTS AND DISCUSSION

Without loss of generality, we first study the properties of HMMs configured as stacked Ag–Si multilayers where the thickness of one Ag–Si pair (t_c) is 20 nm and the filling ratio of Ag in one pair (f_m) is 0.5. The permittivity of Si is fixed as 12.25 [41] and that of Ag is taken from the empirical data [46]. Figure 1(a) shows the real parts of the effective permittivities of in-plane components $\varepsilon_{x/y}$ and out-of-plane component ε_z of the HMM with infinite numbers of Ag–Si pairs based on Maxwell–Garnett effective media theory (see Appendix A). It is seen that $\mathrm{Re}(\varepsilon_{x/y})$ and $\mathrm{Re}(\varepsilon_z)$ have opposite signs in the wavelength range of 1000 to 1400 nm. In detail, $\mathrm{Re}(\varepsilon_{x/y}) < 0$ and $\mathrm{Re}(\varepsilon_z) > 0$ indicate the studied Ag–Si multilayers correspond to a type-II HMM as confirmed by the hyperboloidal IFS given in the right inset of Fig. 1(a). Here we consider a

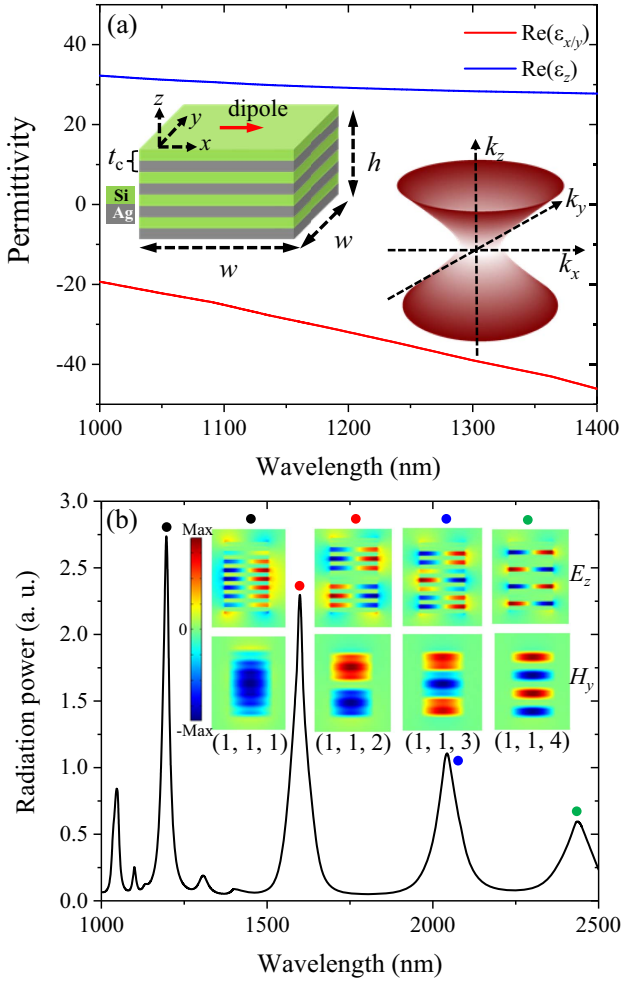

Fig. 1. HMMs and IMCs made of Ag–Si multilayers. (a) Real parts of effective in-pane ($\varepsilon_{x/y}$) and out-of-plane (ε_z) permittivities of the HMM. The IMC made by Ag–Si multilayers and the IFS of the corresponding HMM are shown by the left and right insets, respectively. (b) Spectrum of the radiation power of an x-direction electric dipole close to the IMC. Distributions of the predominate components of near fields of the cavity modes of selected orders.

three-dimensional IMC made of Ag–Si multilayer HMMs with width $w = 100$ nm and height $h = 160$ nm (eight Ag–Si pairs), as sketched by the left inset in Fig. 1(a). Such an IMC supports cavity modes of different orders that can be excited by a near-field source, for example, a point dipole. Figure 1(b) shows the calculated radiation power of an electric point dipole (red arrow) along the x direction located 10 nm away from the center of the top surface of the IMC. The calculation is performed by applying the finite-difference time-domain method (see Appendix B). The spectrum of radiation power shows multiple peaks coming from cavity modes of different orders (m_x, m_y, m_z), where m_i ($i = x, y, z$) indicates the number of field nodes in the i direction. We focus on four dominant peaks labeled by the color dots in Fig. 1(b) and their near-field distributions of E_z (z component of the electric field) and H_y (y component of the magnetic field) on the xoz plane are given by the corresponding insets. According to the near-field

distributions, we can identify these four peaks are attributed to cavity modes of (1, 1, 1), (1, 1, 2), (1, 1, 3), and (1, 1, 4) from short to long wavelength. Here we notice that higher-order modes of the IMC are resonant at longer wavelengths, which is contrary to normal optical cavities. Such an anomalous feature is consistent with previous reports [21,22] and confirms that wave vectors within the proposed IMC bearing hyperbolic dispersion manifested as the same in-plane but larger out-of-plane wave vectors reside at IFSs at lower frequencies (see Appendix C). Another important observation is the labeled modes in Fig. 1(b) regarded as in-plane magnetic multipoles, especially mode (1, 1, 1) that is in fact a y-direction magnetic dipole we will focus on later.

Then, we put a square array of the above IMCs on top of a 300 nm thick Ag mirror and separate them by a SiO_2 (refractive index 1.45 [41]) layer with thickness of s, as sketched by Fig. 2(a). Here, the lattice constant is fixed as $a = 700$ nm and the whole structure is on an infinitely thick SiO_2 substrate and excited by a normally incident plane wave polarized along the x direction. Optical responses of such a resonator-on-mirror structure can be modeled by the temporal coupled mode theory. For simplicity, here we only focus on the coupling between the magnetic dipolar cavity modes (1, 1, 1) in the IMCs and their images in the mirror. In the absence of the Ohmic loss, the Hamiltonian of the system can be expressed as Eq. (1), where ω_0 is the resonant frequency of the uncoupled modes, κ is the near-field coupling coefficient, and k and d are the propagation constant and distance between two modes, respectively:

$$H = \begin{pmatrix} \omega_0 & \kappa \\ \kappa & \omega_0 \end{pmatrix} - i\frac{\gamma_r}{2}\begin{pmatrix} 1 & e^{-ikd} \\ e^{-ikd} & 1 \end{pmatrix}. \tag{1}$$

The eigenvalues of H in Eq. (1) can be obtained as [41,42]

$$\omega_{\pm} = \omega_0 \pm \kappa + i\gamma_r[\pm \exp(ikd) - 1]. \tag{2}$$

Here, only one of the eigenmodes is physically meaningful as a magnetic dipole and its electric-mirror (Ag) image must be in-phase [41,42,47]. According to the mode hybridization theory [48], such in-phase coupling corresponds to the mode with higher energy ω_+. Based on Eq. (2), an ideal Fabry–Pérot BIC is realized if ω_+ becomes a real number, which requires

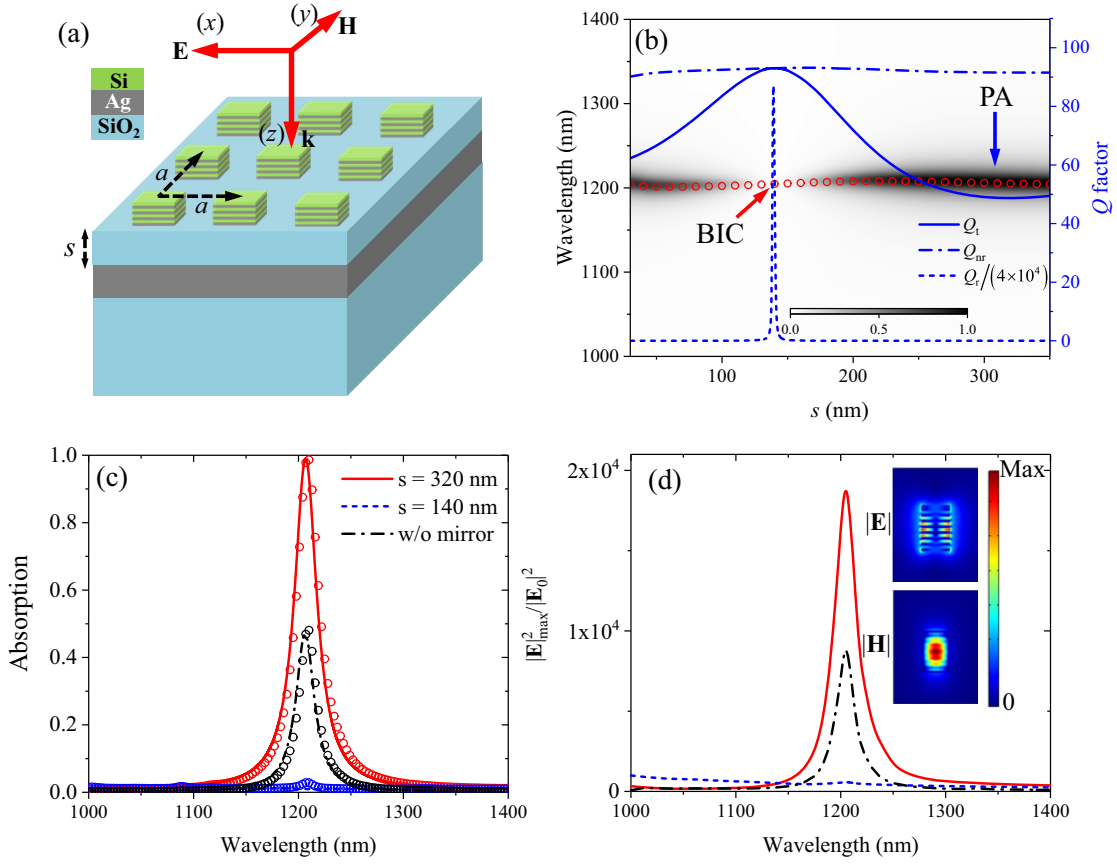

Fig. 2. BIC and PA in IMC arrays coupled to a reflecting mirror. (a) Schematic of the structure of IMC arrays coupled to an Ag mirror. The IMC array has a square lattice with period $a = 700$ nm. The separation between the array and the Ag mirror is determined by the thickness of the SiO_2 spacer (s). The whole structure is excited by a normally incident plane wave. (b) Evolution of absorption spectra, resonance wavelength, and Q factors as a function of s. The positions of BIC and PA are marked by the red and blue arrows. (c) Absorption spectra at the PA point ($s = 320$ nm, red solid line), at the BIC point ($s = 140$ nm, blue dashed line), and without the mirror (black dashed–dotted line). For comparison, the spectra of the cavity made of effective hyperbolic medium are appended as symbols. (d) Spectra of maximum electric field enhancement at the PA point, at the BIC point, and without the mirror. Amplitude distributions of electric and magnetic fields at the absorption peak at the PA point. (d) shares the same legends as (c).

$kd = 2m\pi$ (m is an integer). It is then clear that the structure is able to work at the BIC regime either by tuning k or d, or both. For the propagation constant k, it is determined by $n_{\text{eff}}\omega_0/c$, where n_{eff} is the effective refractive index of the media between two modes and ω_0 is related to the size of the cavity. Here we fix the size of IMCs, and tune d by changing the thickness of the SiO_2 spacer. Figure 2(b) shows the calculated contour map of absorption of the structure as a function of s in the wavelength range of 1000 to 1400 nm. As can be seen, there is a dominant absorption band that evolves as s varies from 30 to 350 nm. In particular, zero absorption appears at $s = 140$ nm (marked by the red arrow), which is exactly a BIC point where the resonance contributing to the absorption cannot be excited by the plane wave. To learn more about this resonance, eigenvalues (resonance wavelengths) and Q factors of this resonance are calculated by applying an eigenfrequency solver based on the finite element method (see Appendix B). As shown by the red circles in Fig. 2(b), eigenvalues match well with the center of the absorption band. Interestingly, the eigenvalues are almost independent on s, which is quite different from other similar structures but with normal cavities such as Si disks or metal–dielectric–metal antennas [35–37]. We argue that this is because the near-field confinement of IMCs is more significant than other normal cavities, yielding negligible κ compared to ω_0 when s is larger than 30 nm. In addition to the total Q factor, Q_t (solid line), Q_r (dashed line), and Q_{nr}(dashed–dotted line) are also calculated (see Appendix B) and appended in Fig. 2(b) to disclose the mechanism of the BIC realized in such a structure. Note that here Q_r is rescaled by $1/(4 \times 10^4)$ for a better visual. As can be seen, Q_t, Q_r, and Q_{nr} show very distinct trends of variation with the change of s. In detail, Q_r increases rapidly when s enters into a narrow range and reaches a very large magnitude at $s = 140$ nm, which is exactly the hallmark of BICs. On the sharp contrast, Q_{nr} is almost independent on s and the magnitude is much smaller than that of Q_r at the BIC point. This observation can be construed by the underlying physics of BIC that it is realized by eliminating the leakage of waves from the structure to far fields, i.e., the radiative loss. On the one hand, for lossless systems such as some all-dielectric structures with negligible Ohmic loss, radiative loss is the only factor that limits the Q value that will become infinitely large at the BIC point [38–40]. Here the finite magnitude of Q_r at the BIC point is caused by the limited size of meshes in the numerical calculation. On the other hand, for most plasmonic systems, for example, the IMC studied here, Ohmic loss must be considered as metals are necessary structural composition. The robustness of Q_{nr} with the change of s confirms that Ohmic loss is irrelevant to the formation of BIC because it is determined by the inherent properties of the mode and the material. Based on the relationship $1/Q_t = 1/Q_r + 1/Q_{nr}$, Q_t of the proposed structure is affected by both Q_r and Q_{nr}, resulting in the overall slow trend of variation with the change of s (see the solid line). When $s = 140$ nm, Q_t reaches maximum (~92) and converges to Q_{nr}, implying that $1/Q_r$ goes to zero and BIC is realized.

Another special point we should notice is the PA point at $s = 320$nm where the absorption is over 0.99. Figure 2(c) shows the absorption spectra of the BIC point $s = 140$ nm (blue dashed line) and the PA point $s = 320$ nm (red solid line). For comparison, the absorption spectrum of the array of IMCs without the Ag mirror is also given as the black dashed–dotted line. Considering the fact that no transmission is allowed due to the optically thick Ag mirror, the incident wave is totally reflected at the BIC point because the cavity mode cannot be excited. As the true BIC condition is broken when $s \neq 140$ nm, the cavity mode is activated, and light is absorbed by the structure. In particular, PA happens when the critical coupling condition is fulfilled, as we will discuss in more detail later. Here we also append the results of the same system but Ag–Si stacked IMCs are replaced by cavities made of effective hyperbolic materials; see symbols in Fig. 2(c). As can be seen, the absorption spectra of the IMC arrays made of Ag–Si layers and effective hyperbolic materials are almost overlapped, indicating the hyperbolic nature of IMCs is kept in the BIC regime. Figure 2(d) shows the spectra of the maximum electric near-field enhancement defined as $|\mathbf{E}|^2_{\text{max}}/|\mathbf{E}_0|^2$ ($\mathbf{E}$ is the electric field of the structure under excitation and $\mathbf{E}_0$ is that of the incident wave) for the structure at the PA point (red solid line), at the BIC point (blue dashed line), and without the mirror (black dashed–dotted line). It shows that the maximum near-field enhancement exceeds 1.8×10^4 at the resonance of the PA point due to the ultra-strong field confinement of IMCs. The amplitude distributions of electric and magnetic fields are shown by the insets in Fig. 2(d), which confirms that the resonance is the magnetic dipolar mode (1, 1, 1).

To get a deep understanding of the BIC and the PA points, in Fig. 3(a) we show the calculated total damping rate γ_t (black solid line), radiative damping rate γ_r (blue dashed line), and nonradiative damping rate γ_{nr} (red dashed–dotted line) of the structure as a function of s (see Appendix B). Clearly, γ_{nr} is nearly independent on s as it is mainly determined by the Ohmic loss of metals in the structure. In contrast, γ_r is strongly affected by s and vanishes at $s = 140$ nm, i.e., at the BIC point. As a consequence, the total damping rate (γ_t) of the structure declines to γ_{nr} at the BIC point as marked by the red arrow. Meanwhile, the PA point (see the blue arrow) corresponds to the position where γ_r is nearest to γ_{nr}, implying the condition of critical coupling is almost satisfied. Based on the temporal coupled mode theory, the absorption of the structure can be obtained by Eq. (3) [41,49]:

$$A = \frac{4\gamma_r\gamma_{nr}}{(\omega - \omega_0)^2 + \gamma_t^2}. \tag{3}$$

The condition of critical coupling refers to $\gamma_r = \gamma_{nr}$ where the absorption A reaches 100% at $\omega = \omega_0$. As shown in Fig. 3(b), the calculated absorption spectrum based on Eq. (3) agrees well with the numerical result. Note that although the condition of critical coupling is not perfectly met according to the results shown in Fig. 3(a), the absorption can still surpass 0.99 near the PA point since γ_r is very close to γ_{nr} when s is in the range of 270 to 350 nm.

Next, we investigate how to modulate optical responses of the structure by geometries and material compositions. Figures 4(a) and 4(b) show the evolution of absorption spectra as a function of s for the structure with $w = 80$ nm and $w = 120$ nm, respectively. Shrinking (expanding) IMCs in

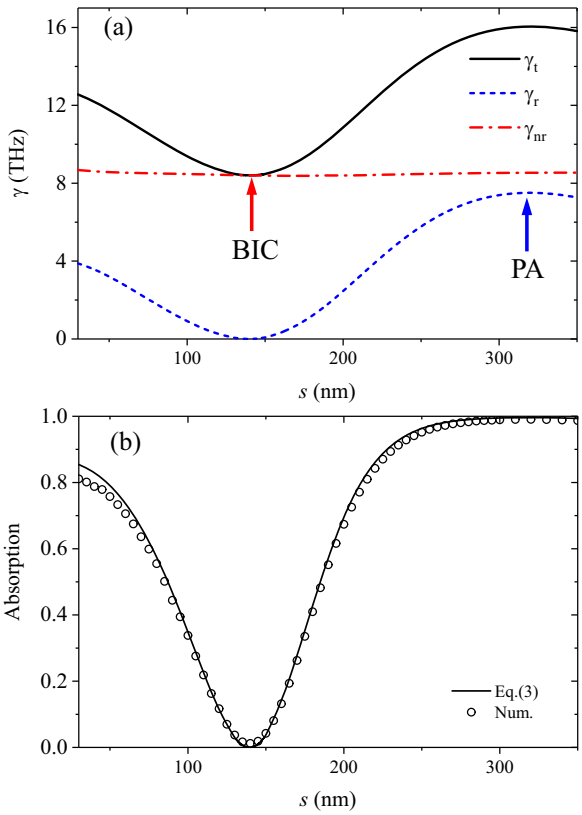

Fig. 3. Damping rates and PA realized due to critical coupling. (a) Total damping rate γ_t, radiative damping rate γ_r, and nonradiative damping rate γ_{nr} as a function of s. (b) Comparison between the absorption spectra obtained by Eq. (3) and numerical calculations.

the x and y directions results in resonance of cavity mode (1, 1, 1) at shorter (longer) wavelength as can be seen from the shift of absorption bands. At the same time, the BIC points also appear at different s because the propagating constant (k) between two coupled modes changes due to different resonance frequency. In addition, the structure with $w = 80$ nm shows the narrowest absorption band compared to those of $w = 100$ nm [Fig. 2(b)] and $w = 120$ nm [Fig. 4(b)], indicating a high Q factor. The reason for the increased Q factor may come from two aspects. First, volume of metals is reduced in smaller IMCs, resulting in less nonradiative damping; second, the radiative Q factor (Q_r) of IMCs is inversely proportional to the fourth power of the characteristic length L, i.e., $Q \propto L^{-4}$ [21], where $L = V^{1/3}$ and V is the volume of the cavity. To study the structure with IMCs of different height h, we plot the absorption contour maps of the structure with 6 ($h = 120$ nm) and 10 ($h = 200$ nm) Ag–Si pairs in Fig. 4(c) and Fig. 4(d), respectively. It shows that the absorption band of the structure with thinner (thicker) IMCs locates at the longer (shorter) wavelength. This resonance shift is apparently opposite to the case for cavities made of normal materials, further confirming mirror coupled IMCs still bear the nature of HMMs. The anomalous resonance shift is consistent with the result shown in Fig. 1(b) that both can be understood by analyzing the unique IFSs of HMMs (see Appendix C). Similar to result of Fig. 4(a), smaller cavities have a narrower absorption band. However, one should keep in mind that the number of Ag–Si pairs cannot be too small, otherwise the Ag–Si multilayers will deviate from the effective HMM. Another parameter we want to discuss is the filling ratio (f_m) of Ag because it is the only degree of freedom to tune the effective permittivity tensor of Ag–Si multilayer HMMs (see Appendix A). Figures 4(e) and 4(f) are the plots of absorptions

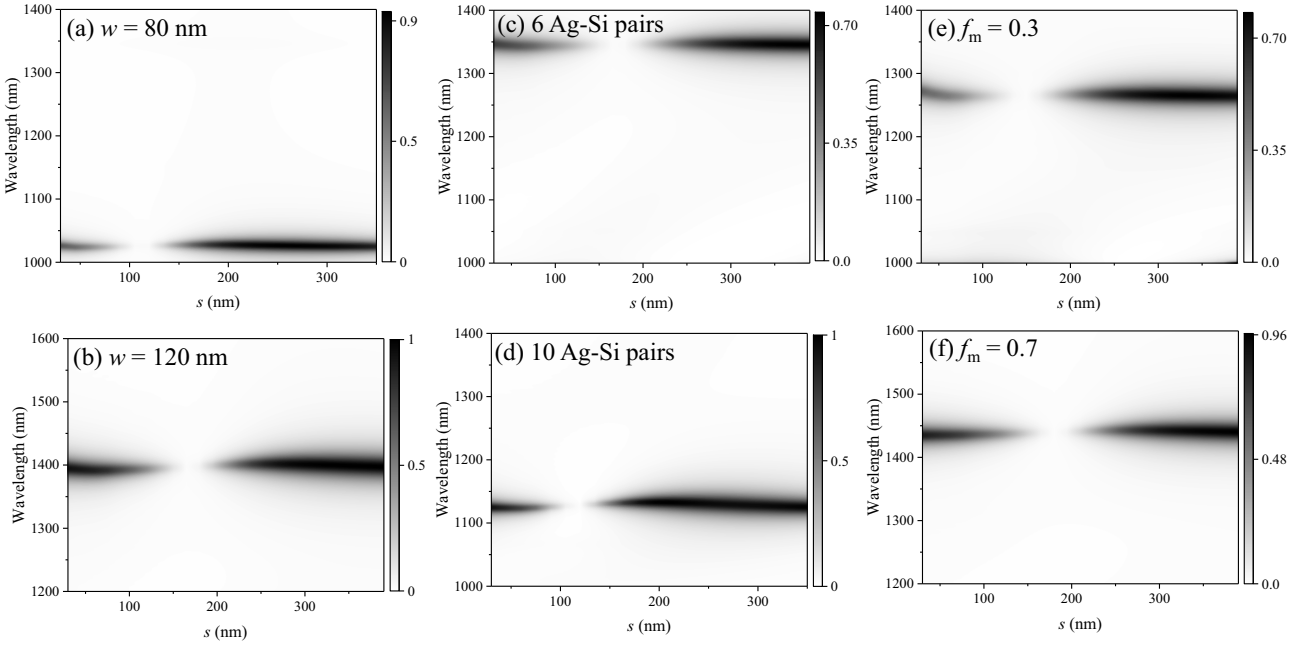

Fig. 4. Absorption maps as a function of wavelength and s for mirror coupled IMCs with different parameters. (a) $w = 80$ nm, (b) $w = 120$ nm, (c) 6 Ag–Si pairs, (d) 10 Ag–Si pairs, (e) $f_m = 0.3$, and (f) $f_m = 0.7$. Other parameters are the same as those in Fig. 2.

for the structure with $f_m = 0.3$ and $f_m = 0.7$, respectively, which show absorption bands at different wavelengths. This resonance tuning property is readily understood by the variation of IFSs of HMMs with different permittivity tensors. Note that there is a limited range of f_m (about 0.2 to 0.8) for the Ag–Si multilayers that can be treated as a type-II HMM in the wavelength range from 1000 to 1600 nm. Out of this range, the Ag–Si multilayers will degenerate to either effective dielectrics ($f_m < 0.2$) or effective metals ($f_m < 0.8$) (see Appendix A). Overall, results in Fig. 4 show flexible tuning of the optical responses of mirror coupled IMCs while BICs are robust for different parameters. However, one may find that not all the structures in Fig. 4 present features of PA in the considered space of parameters (see the upper limits of color bars). Interestingly, it seems that PA is more likely to be realized in structures with larger volume of metals as in Figs. 4(b), 4(d), and 4(f). Moreover, results in Fig. 4 indicate that it is possible to obtain PA with perfectly matched γ_r and γ_{nr} by adjusting the geometry and material compositions of the structure. For example, the maximum absorption of the structure with $w = 120$ nm shown in Fig. 4(b) is larger than 0.9999 as the calculated relative difference $|\gamma_{nr} - \gamma_r|/\gamma_{nr}$ is less than 5%.

After the analysis of the BIC and PA realized in mode (1, 1, 1), we investigate more about the mirror coupled IMCs by surveying the mode characteristics of three higher-order modes that are mode (1, 1, 2), mode (1, 1, 3), and mode (1, 1, 4). In Fig. 5(a), we show the absorption and reflection spectra of the structure under the excitation of a plane wave in the wavelength range from 1400 to 2450 nm. It is seen that the absorption (reflection) spectrum shows three peaks (dips) of which the resonance wavelengths are in accordance with those of mode (1, 1, 2), mode (1, 1, 3), and mode (1, 1, 4) shown in Fig. 1(b) in turn. However, it is noted that all the absorption peaks are extremely tiny (smaller than 0.02) while the overall reflection is larger than 0.98, indicating that the excitation of those higher-order modes by a plane wave is quite weak compared to that of mode (1, 1, 1), as shown in Fig. 2(c). This observation can be construed by the fact that these higher-order modes are actually "dark modes" to a far-field source such as a plane wave. From the distributions of H_y shown in the insets of Fig. 1(b), we can regard these higher-order modes as resonances with multiple magnetic dipoles in opposite phases, leading to nearly zero net dipole moment. Therefore, it is not possible to realize perfect absorption by these higher-order modes. However, we stress that these "dark modes" can be efficiently excited by a near-field source (e.g., a dipole), as shown in Fig. 1(b). The resonance wavelengths and Q factors of these modes as functions of s are further calculated and shown in Fig. 5(b). As can be seen, both the resonance wavelengths and Q factors of these modes are inert to s and no sign of BIC can be identified. To present a more detailed analysis, in Fig. 5(c) we show the evolution of γ_r and γ_{nr} of these modes with the change of s. It is seen that γ_{nr} is much larger than γ_r (2 orders of magnitude at least) for all these modes, which is quite different from the case of mode (1, 1, 1), as shown in Fig. 3(a). This further verifies that these higher-order modes barely radiate to far fields and their Ohmic loss is quite strong. Interestingly, mode (1, 1, 3) exhibits a hallmark of BIC by noticing that γ_r almost vanishes at the dip at $s \approx 270$ nm. Nevertheless, such BIC is meaningless as γ_{nr} dominates the damping, resulting in no significant enhancement of the total Q factor by this BIC, as can be seen in Fig. 5(b).

In the final discussion, we want to give a brief demonstration of the enhanced lighter–matter interactions by combining BICs and IMCs. At the BIC point, the fields of the mode (1, 1, 1) are strongly confined within the cavity and do not contribute to far-field radiation but can leak to the near-field regime. The strong light–matter interaction at nanoscale can be realized in regions within or very close to IMCs. One of the most common effects due to the strong light–matter interactions is the enhancement of spontaneous emission rate of quantum emitters, known as the Purcell effect. Experimental demonstrations of strong light–matter interactions related to the Purcell effect have been realized by spin coating quantum dots on IMC arrays [14,15] or doping laser dye in the dielectric layers of HMMs [50]. Theoretically, the Purcell effect can be investigated by calculating the Purcell factor of the structure. To this end, in Fig. 6(a) we show the calculated spectra of the Purcell factor of the mirror coupled IMC arrays with varying s. Here, the calculation is carried out for an electric dipole along the x direction located 10 nm away from the center of the top surface of the center IMC in a structure containing 5 × 5 arrays.

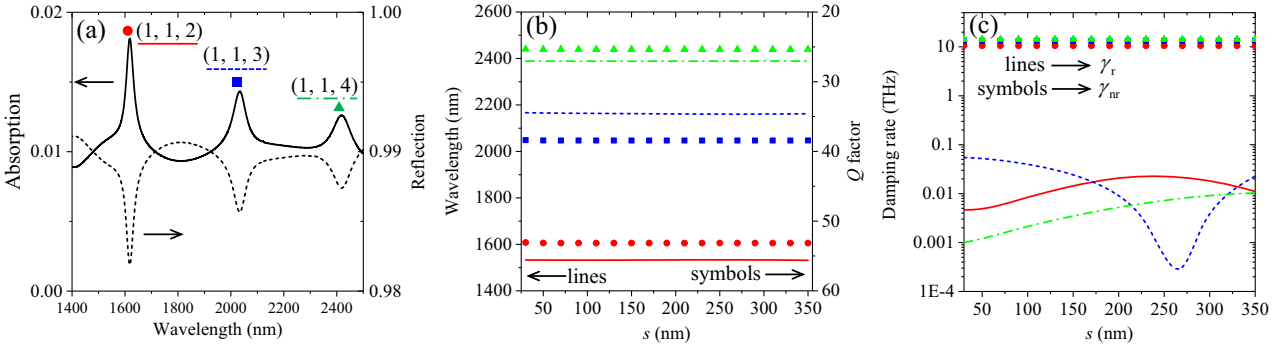

Fig. 5. Mode characteristics of mode (1, 1, 2), mode (1, 1, 3), and mode (1, 1, 4). (a) Absorption (left y axis) and reflection (right y axis) spectra of the structure in the wavelength range from 1400 to 2450 nm. The absorption peaks of mode (1, 1, 2), mode (1, 1, 3), and mode (1, 1, 4) are marked by red dot (red solid line), blue square (blue dashed line), and green triangle (green dashed–dotted line), in turn. (b) Resonance wavelengths (lines) and Q factors (symbols) as a function of s. (c) γ_r (lines) and γ_{nr} (symbols) as a function of s. The styles of lines and symbols in (b) and (c) are in accordance with those markers in (a) for different modes.

The Purcell factor is obtained by calculating the ratio P_{dip}/P_0, where P_{dip} is the radiative power of the dipole close to the structure and P_0 is that when the structure is absent. As can be seen, all the spectra of the Purcell factor show peaks with the Purcell factor larger than 80 at about 1200 nm, which is exactly the resonance wavelength of the cavity mode (1, 1, 1). This indicates that the proposed structure is a good platform to realize spontaneous emission-rate enhancement. This can be understood by the fact that the Purcell factor of a nanocavity is actually proportional to Q/V_m [14–16]. In our structure, V_m of the mode (1, 1, 1) at the BIC point is calculated as small as $4.627 \times 10^{-5}\ \lambda_0^3$ (λ_0 is the resonance wavelength of the mode; see Appendix B), which evidently confirms the extremely small mode volume of the IMC due to the large wavenumber in HMMs. As a result, Q/V_m is still as large as $1.945 \times 10^6\ \lambda_0^{-3}$ although the Q factor of the IMC (~92 at the BIC point) cannot compete with that of lossless structures. More importantly, the mirror coupled structure presents an additional degree of freedom to tune the Purcell enhancement as we can see that peak values of the spectra of the Purcell factor are dependent on s. To unravel the relation between the Purcell enhancement and s, we plot peak values of the Purcell factor as a function of s in Fig. 6(b). Note that here Purcell factors are normalized to the peak value of the IMC array without the mirror. It shows that the trend of the Purcell factor evolving as s is quite similar to that of Q factors shown in Fig. 2(b). The maximum Purcell factor appears at about $s = 175$ nm that is slightly deviated from the BIC point $s = 140$ nm. This discrepancy comes from the finite number of arrays in the calculation (5×5) as running simulation models of more arrays is out of memory of our computation resources. Notwithstanding, the result in Fig. 6(b) is strong evidence that the Purcell effect of IMCs can be further enhanced by BICs by noticing that the maximum of the normalized Purcell factor can be larger than 1.4. We believe this enhancement could be more significant in systems with enough arrays where wave leaking from structure boundary can be ignored.

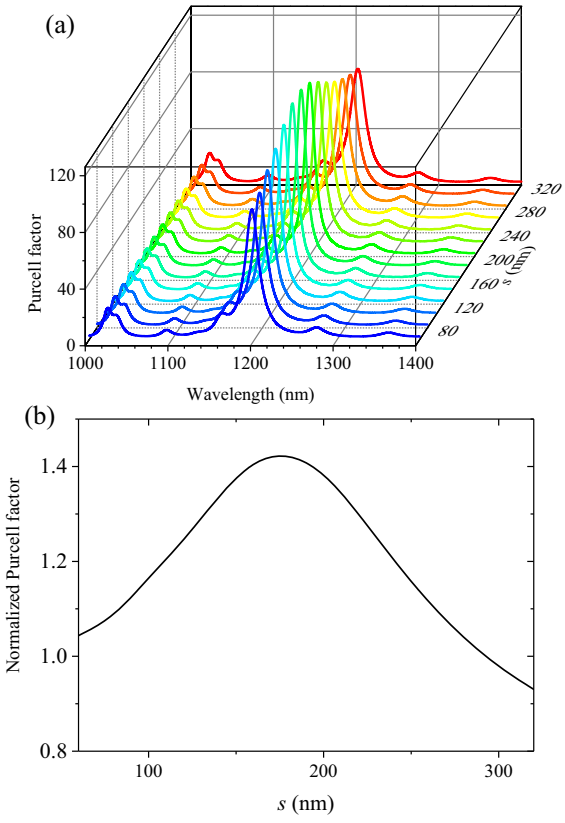

Fig. 6. Enhancement of Purcell effect by BICs in mirror coupled IMC arrays. (a) Spectra of Purcell factor of the structures for different s. (b) Normalized Purcell factor as a function of s.

3. CONCLUSION

In summary, we have shown that arrays of IMCs coupled to a metal mirror can work under the framework of BICs while keeping the intriguing features of hyperbolic HMMs. The Q factor of IMCs can be effectively enlarged at the BIC point by completely quenching the radiative loss. Similar to other structures applying normal cavities, PA can also be realized but the resonance shows an anomalous scaling law with respect to the cavity size. Optical responses of the proposed structure can be flexibly tuned not only by the geometry of the cavity but also the filling ratio of metals. The ratio between the mode volume and the Q factor of IMCs is further increased, leading to a significant enhancement of Purcell factor. The proposed structure can be fabricated in experiments by applying advanced technologies of lift-up and lithography such as electron-beam evaporation, electron-beam or focused ion beam lithography. There have been many experimental studies on both IMCs and mirror coupled resonators demonstrating the good agreement between measured and calculated results, though some deviations may arise due to the defects of fabricated samples [15,22,42]. The calculated results presented in this work contribute solid theoretical cornerstones to future experimental studies. The idea that combining IMCs and BICs is not limited to the structure studied in this work and can be extended to other systems applying different types of IMCs, for example, nanowire arrays, and different types of BICs, for example, symmetry-protected BICs. In addition, there have been several strategies to overcome Ohmic loss of metals in optical nanocavities including gain compensation and low temperature environment [51–53]. We believe our results promote the applications of IMCs in nonlinear optics, light-harvesting devices, spontaneous emission engineering, strong coupling systems, and so on.

APPENDIX A: MAXWELL–GARNETT THEORY

HMMs made of stacked metal–dielectric layers can be considered as a homogeneous effective medium with a uniaxial permittivity tensor. If metal–dielectric layers are stacked in the z direction, then the principal components of the permittivity tensor can be obtained by the Maxwell–Garnett theory [18–20]:

$$\varepsilon_{x/y} = f_m\varepsilon_m + (1 - f_m)\varepsilon_d,$$
$$\varepsilon_z = \frac{\varepsilon_m\varepsilon_d}{(1 - f_m)\varepsilon_m + f_m\varepsilon_d}, \tag{A1}$$

where ε_m and ε_d are the permittivity of metal and dielectric, respectively. HMMs can be categorized to type-I and type-II

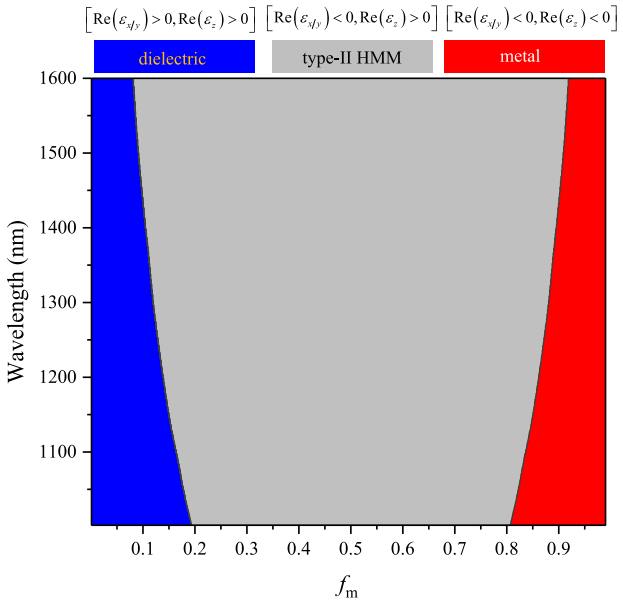

Fig. 7. Optical phase diagram of the effective medium made of stacked Ag–Si multilayers.

that correspond to $\mathrm{Re}(\varepsilon_{x/y})>0$, $\mathrm{Re}(\varepsilon_z)<0$ and $\mathrm{Re}(\varepsilon_{x/y})<0$, $\mathrm{Re}(\varepsilon_z)>0$, respectively. Based on Eq. (A1), the optical phase diagram of the effective medium is shown in Fig. 7 from which we can see that the stacked Ag–Si multilayers can be treated as type-II HMMs as long as $0.2<f_m<0.8$ in the wavelength range of 1000 to 1600 nm. Strictly speaking, Eq. (A1) is accurate only when the metal–dielectric pair is infinitely thin, i.e., $t_c \to 0$. Although there have been more precise equations that incorporate the corrections related to t_c [54,55], Eq. (A1) can be valid as long as t_c is small enough to ensure the metal–dielectric multilayers can be regarded as a homogenous effective medium. In addition, a finitely thick metal–dielectric pair will put an upper limit to the wavenumber of HMMs given by $2\pi/t_c$ which is much larger than the corresponding wavenumber in vacuum [14].

APPENDIX B: NUMERICAL METHOD

Numerical results of absorption spectra, radiation power, and Purcell factors of electric dipoles were calculated by using the finite-difference time-domain method. In all the simulations, the global mesh accuracy was set as 8 per wavelength and mesh sizes of regions containing IMCs were set as 1 nm to ensure the accuracy of results. For the calculation of radiative power and Purcell factors, perfectly matched layers (PMLs) were applied in the x, y, and z directions to avoid unphysical reflections from the simulation boundaries. For the calculation of absorption (reflection) spectra under the excitation of a normally incident plane wave, a single unit cell with periodic boundary conditions in the x and y directions, and PMLs in the z direction were applied. Eigenvalues and Q factors were calculated by using an eigenfrequency solver based on the finite element method. Except for PMLs in the z direction, Floquet periodic conditions were used in the x and y directions with $k_{Fx}=k_{Fy}=0$, where k_{Fx} (k_{Fy}) is the x (y) component of k-vector for Floquet periodicity. Meshes were refined until eigenvalues and Q factors reached convergence.

To calculate γ_r and Q_r, the imaginary part of the permittivity of Ag was set as zero in the eigenfrequency solver. Then, γ_{nr} and Q_{nr} can be obtained based on $\gamma_t=\gamma_r+\gamma_{nr}$ and $1/Q_t=1/Q_r+1/Q_{nr}$, respectively. The mode volume V_m was calculated based on the following equations [22]:

$$V_m=\frac{\iiint W(\mathbf{r})\mathrm{d}^3r}{\max[W(\mathbf{r})]}, \tag{B1}$$

$$W(\mathbf{r})=\frac{1}{2}\left\{\mathrm{Re}\left[\frac{\mathrm{d}(\omega\varepsilon)}{\mathrm{d}\omega}\right]|\mathbf{E}(\mathbf{r})|^2+\mu|\mathbf{H}(\mathbf{r})|^2\right\}, \tag{B2}$$

where $W(\mathbf{r})$ is the local electromagnetic energy density at position $\mathbf{r}$, ε and μ are the local permittivity and permeability, respectively, and the integration is executed over the entire space. $\mathbf{E}(\mathbf{r})$ and $\mathbf{H}(\mathbf{r})$ are the local electric and magnetic fields, respectively, calculated by the eigenfrequency solver.

APPENDIX C: IFSS OF HMMS AND ANOMALOUS SCALING LAW OF IMCS

In a uniaxial medium, the equation of IFS for the TM-polarized wave can be expressed as

$$\frac{k_x^2+k_y^2}{\varepsilon_{zz}}+\frac{k_z^2}{\varepsilon_{x/y}}=k_0^2, \tag{C1}$$

where k_0 is the magnitude of wave vector in vacuum, and k_i ($i=x,y,z$) is the i component of the wave vector in the medium. Based on Eq. (C1), Fig. 8 shows the cross-section view of the IFSs of Ag–Si HMMs ($f_m=0.5$) and a normal material (Si, $\varepsilon_{zz}=\varepsilon_{x/y}=12.25$) on the k_x-k_z plane for a

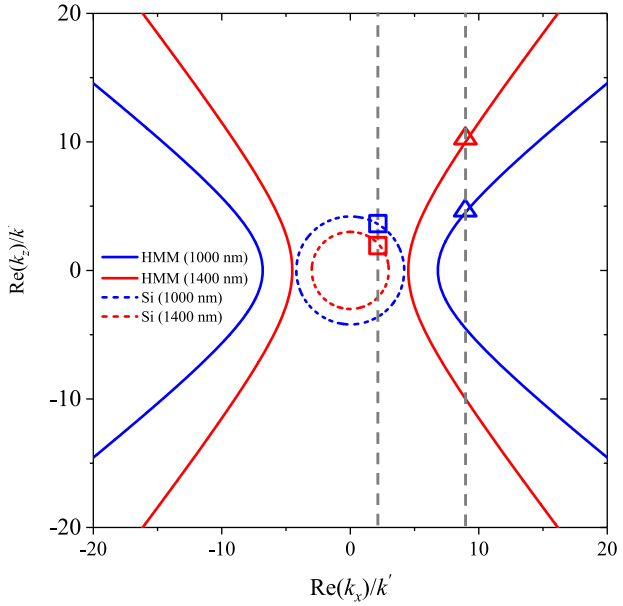

Fig. 8. Cross-section view of the IFSs of Ag–Si HMMs ($f_m=0.5$) and Si on the k_x-k_z plane for a short and a long wavelength. k' is the magnitude of a reference wave vector which is set as $2\pi/1200$ nm. The vertical dashed lines are guide for fixed k_x.

shorter (1000 nm) and a longer wavelength (1400 nm). As can be seen, the IFSs of HMMs exhibit hyperbolic shape which is totally different from that of a normal material that is a closed sphere. More importantly, the IFS of HMMs at a longer wavelength (red solid line) is flatter than that of a shorter wavelength (blue solid line). As a result, a larger (smaller) k_z resides at the IFS of a longer (shorter) wavelength for a fixed in-plane wave vector as marked by the red (blue) upward-triangle. This is opposite to the case of a normal material, for example, Si, as shown by the dashed circles and boxes.

A cavity mode of order (m_x, m_y, m_z) in cuboid IMCs is formed when the round-trip phases of optical waves propagating along x, y, and z are integer multiples of 2π, i.e.,

$$\begin{aligned} 2k_xL_x + \Delta\varphi_x &= 2m_x\pi, \\ 2k_yL_y + \Delta\varphi_y &= 2m_y\pi, \\ 2k_zL_z + \Delta\varphi_z &= 2m_z\pi. \end{aligned} \tag{C2}$$

Here L_i $(i = x, y, z)$ is the cavity length in the i direction, and $\Delta\varphi_i$ $(i = x, y, z)$ represents the phase shift in the i direction caused by the reflection at cavity–air interfaces. For cavity modes of different orders in an IMC with fixed size, such as those modes labeled in Fig. 1(b), the mode orders in the x and y directions are $m_x = m_y = 1$, which means k_x and k_y of optical waves are fixed for these modes. Meanwhile, k_z has to increase for a mode of higher order in the z direction, i.e., a larger m_z based on Eq. (C2). Similar discussion can be applied for cavity modes of the same orders but with different cavity size in the z direction compared to the case in Figs. 4(c) and 4(d). A thinner cavity (smaller L_z) with a smaller number of Ag–Si pairs results in larger k_z. Then the anomalous scaling law of resonance wavelength of cavity modes in IMCs can be comprehended according to the IFSs shown in Fig. 8 as larger k_z at the same k_x and k_y locates on the IFS of longer wavelength.

Funding. National Natural Science Foundation of China (12004273, 11574228, 11874276, 61905113); Key Research and Development Program of Shanxi Province (201903D121131).

Disclosures. The authors declare no conflicts of interest.

Data Availability. Data underlying the results presented in this paper are not publicly available at this time but may be obtained from the authors upon reasonable request.

REFERENCES

1. Y. M. Liu and X. Zhang, "Metamaterials: a new frontier of science and technology," Chem. Soc. Rev. **40**, 2494–2507 (2011).
2. N. I. Zheludev and Y. S. Kivshar, "From metamaterials to metadevices," Nat. Mater. **11**, 917–924 (2012).
3. T. Koschny, C. M. Soukoulis, and M. Wegener, "Metamaterials in microwaves, optics, mechanics, thermodynamics, and transport," J. Opt. **19**, 084005 (2017).
4. P. T. Xie, Z. C. Shi, M. Feng, *et al.*, "Recent advances in radio-frequency negative dielectric metamaterials by designing heterogeneous composites," Adv. Compos. Hybrid Mater. **5**, 679–695 (2022).
5. V. M. Shalaev, "Optical negative-index metamaterials," Nat. Photonics **1**, 41–48 (2007).
6. D. R. Smith, J. B. Pendry, and M. C. K. Wiltshire, "Metamaterials and negative refractive index," Science **305**, 788–792 (2004).
7. P. Moitra, Y. M. Yang, Z. Anderson, *et al.*, "Realization of an all-dielectric zero-index optical metamaterial," Nat. Photonics **7**, 791–795 (2013).
8. N. Kinsey, C. DeValut, A. Boltasseva, *et al.*, "Near-zero-index materials for photonics," Nat. Rev. Mater. **4**, 742–760 (2019).
9. K. Wang, S. H. Park, J. T. Zhu, *et al.*, "Self-assembled colloidal nanopatterns toward unnatural optical meta-materials," Adv. Funct. Mater. **31**, 2008246 (2021).
10. X. F. Jing, Y. N. Xu, H. Y. Gan, *et al.*, "High refractive index metamaterials by using higher order modes resonances of hollow cylindrical nanostructure in visible region," IEEE Access **7**, 144945 (2019).
11. S. B. Glybovski, S. A. Tretyakov, P. A. Belov, *et al.*, "Metasurfaces: from microwaves to visible," Phys. Rep. **634**, 1–72 (2016).
12. J. Kim, J. Seong, Y. Yang, *et al.*, "Tunable metasurfaces towards versatile metalenses and metaholograms: a review," Adv. Photon. **4**, 024001 (2022).
13. A. Poddubny, I. Iorsh, P. Belov, *et al.*, "Hyperbolic metamaterials," Nat. Photonics **7**, 948–957 (2013).
14. S. R. K. C. Indukuri, J. Bar-David, N. Mazurski, *et al.*, "Ultrasmall mode volume hyperbolic nanocavities for enhanced light–matter interaction at the nanoscale," ACS Nano **13**, 11770–11780 (2019).
15. D. Lu, J. J. Kan, E. E. Fullerton, *et al.*, "Enhancing spontaneous emission rates of molecules using nanopatterned multilayer hyperbolic metamaterials," Nat. Nanotechnol. **9**, 48–53 (2014).
16. C. Guclu, T. S. Luk, G. T. Wang, *et al.*, "Radiative emission enhancement using nano-antennas made of hyperbolic metamaterial resonators," Appl. Phys. Lett. **105**, 123101 (2014).
17. L. Lu, R. E. Simpson, and S. K. Valiyaveedu, "Active hyperbolic metamaterials: progress, materials and design," J. Opt. **20**, 103001 (2018).
18. P. Shekhar, J. Atkinson, and Z. Jacob, "Hyperbolic metamaterials: fundamentals and applications," Nano Convergence **1**, 14 (2014).
19. L. Ferraria, C. Wub, D. Lepaged, *et al.*, "Hyperbolic metamaterials and their applications," Prog. Quantum Electron. **40**, 1–40 (2015).
20. A. Aigner, J. M. Dawes, S. A. Maier, *et al.*, "Nanophotonics shines light on hyperbolic metamaterials," Light Sci. Appl. **11**, 9 (2022).
21. J. Yao, X. D. Yang, X. B. Yin, *et al.*, "Three-dimensional nanometer-scale optical cavities of indefinite medium," Proc. Natl. Acad. Sci. USA **108**, 11327–11331 (2011).
22. X. D. Yang, J. Yao, J. Rho, *et al.*, "Experimental realization of three-dimensional indefinite cavities at the nanoscale with anomalous scaling laws," Nat. Photonics **6**, 450–454 (2012).
23. Y. Q. Zhao, A. Hubarevich, M. Iarossi, *et al.*, "Hyperbolic nanoparticles on substrate with separate optical scattering and absorption resonances: a dual function platform for SERS and thermoplasmonics," Adv. Opt. Mater. **9**, 2100888 (2021).
24. H. F. Xu, Z. M. Zhu, J. C. Xue, *et al.*, "Giant enhancements of high-order upconversion luminescence enabled by multiresonant hyperbolic metamaterials," Photon. Res. **9**, 395–404 (2021).
25. N. Maccaferri, A. Zilli, T. Isoniemi, *et al.*, "Enhanced nonlinear emission from single multilayered metal–dielectric nanocavities resonating in the near-infrared," ACS Photon. **8**, 512–520 (2021).
26. Y. R. He, H. X. Deng, X. Y. Jiao, *et al.*, "Infrared perfect absorber based on nanowire metamaterial cavities," Opt. Lett. **38**, 1179–1181 (2013).
27. D. X. Ji, H. M. Song, X. Zeng, *et al.*, "Broadband absorption engineering of hyperbolic metafilm patterns," Sci. Rep. **4**, 4498 (2014).
28. R. Chandrasekar, Z. X. Wang, X. G. Meng, *et al.*, "Lasing action with gold nanorod hyperbolic metamaterials," ACS Photon. **4**, 674–680 (2017).
29. K.-C. Shen, C.-T. Ku, C. Hsieh, *et al.*, "Deep-ultraviolet hyperbolic metacavity laser," Adv. Mater. **30**, 1706918 (2018).
30. Z. W. Guo, H. T. Jiang, and H. Chen, "Zero-index and hyperbolic metacavities: fundamentals and applications," J. Phys. D **55**, 083001 (2022).
31. R. Y. Liu, C. L. Zhou, Y. Zhang, *et al.*, "Near-field radiative heat transfer in hyperbolic materials," Int. J. Extrem. Manuf. **4**, 032002 (2022).
32. B. A. Liu and S. Shen, "Broadband near-field radiative thermal emitter/absorber based on hyperbolic metamaterials: direct numerical

simulation by the Wiener chaos expansion method," Phys. Rev. B **87**, 115403 (2013).
33. S. R. K. C. Indukuri, C. Frydendahl, J. Bar-David, *et al.*, "WS_2 monolayers coupled to hyperbolic metamaterial nanoantennas: broad implications for light-matter-interaction applications," ACS Appl. Nano Mater. **3**, 10226–10233 (2020).
34. X. T. Yu, Y. F. Yuan, J. H. Xu, *et al.*, "Strong coupling in microcavity structures: principle, design, and practical application," Laser Photon. Rev. **13**, 1800219 (2019).
35. C. W. Hsu, B. Zhen, A. D. Stone, *et al.*, "Bound states in the continuum," Nat. Rev. Mater. **1**, 16048 (2016).
36. K. Koshelev, A. Bogdanov, and Y. Kivshar, "Meta-optics and bound states in the continuum," Sci. Bull. **64**, 836–842 (2019).
37. S. I. Azzam and A. V. Kildishev, "Photonic bound states in the continuum: from basics to applications," Adv. Opt. Mater. **9**, 2001469 (2020).
38. K. Koshelev, S. Lepeshov, M. K. Liu, *et al.*, "Asymmetric metasurfaces with high-*Q* resonances governed by bound states in the continuum," Phys. Rev. Lett. **121**, 193903 (2018).
39. F. Wu, J. J. Wu, Z. W. Guo, *et al.*, "Giant enhancement of the Goos-Hänchen shift assisted by quasibound states in the continuum," Phys. Rev. Appl. **12**, 014028 (2019).
40. F. Wu, T. T. Liu, Y. Long, *et al.*, "Giant photonic spin Hall effect empowered by polarization-dependent quasibound states in the continuum in compound grating waveguide structures," Phys. Rev. B **107**, 165428 (2023).
41. X. Y. Zong, L. X. Li, and Y. F. Liu, "Bound states in the continuum enabling ultra-narrowband perfect absorption," New J. Phys. **25**, 023020 (2023).
42. G. C. Yang, S. U. Dev, M. S. Allen, *et al.*, "Optical bound states in the continuum enabled by magnetic resonances coupled to a mirror," Nano Lett. **22**, 2001–2008 (2022).
43. Z. Wang, Y. Liang, J. Q. Qu, *et al.*, "Plasmonic bound states in the continuum for unpolarized weak spatially coherent light," Photon. Res. **11**, 260–269 (2023).
44. X. Xiao, Y. X. Lu, J. Y. Jiang, *et al.*, "Manipulation of optical bound states in the continuum in a metal-dielectric hybrid nanostructure," Photon. Res. **10**, 2526–2531 (2022).
45. L. D. Zhou, M. Panmai, S. L. Li, *et al.*, "Lighting up Si nanoparticle arrays by exploiting the bound states in the continuum formed in a Si/Au hybrid nanostructure," ACS Photon. **9**, 2991–2999 (2022).
46. P. B. Johnson and R. W. Christy, "Optical constants of the noble metals," Phys. Rev. B **6**, 4370–4379 (1972).
47. E. X. Perez, L. Shi, and U. Tuzer, "Mirror-image-induced magnetic modes," ACS Nano **7**, 664–668 (2013).
48. P. Nordlander, C. Oubre, E. Prodan, *et al.*, "Plasmon hybridization in nanoparticle dimers," Nano Lett. **4**, 899–903 (2004).
49. J. Yoon, K. H. Seol, S. H. Song, *et al.*, "Critical coupling in dissipative surface-plasmon resonators with multiple ports," Opt. Express **18**, 25702–25711 (2010).
50. T. Tumkur, G. Zhu, P. Black, *et al.*, "Control of spontaneous emission in a volume of functionalized hyperbolic metamaterial," Appl. Phys. Lett. **99**, 151115 (2011).
51. I. D. Leon and P. Berini, "Amplification of long-range surface plasmons by a dipolar gain medium," Nat. Photonics **4**, 382–387 (2010).
52. X. Ni, S. Ishii, M. D. Thoreson, *et al.*, "Loss-compensated and active hyperbolic metamaterials," Opt. Express **19**, 25242–25254 (2011).
53. Y. Y. Gonga and J. Vučković, "Design of plasmon cavities for solid-state cavity quantum electrodynamics applications," Appl. Phys. Lett. **90**, 033113 (2007).
54. J. Kim, V. P. Drachev, Z. Jacob, *et al.*, "Improving the radiative decay rate for dye molecules with hyperbolic metamaterials," Opt. Express **20**, 8100–8116 (2012).
55. O. Kidwai, S. V. Zhukovsky, and J. E. Sipe, "Effective-medium approach to planar multilayer hyperbolic metamaterials: strengths and limitations," Phys. Rev. A **85**, 053842 (2012).